



Evaluation of oxygen separation from air by pressure/vacuum swing adsorption

Gabriel Jesus de Almeida Henrique¹ · Antônio Eurico Belo Torres¹ · Diana Cristina Silva de Azevedo¹ · Rafael Barbosa Rios² · Moisés Bastos-Neto¹

Received: 7 June 2023 / Revised: 29 September 2023 / Accepted: 23 February 2024 / Published online: 9 April 2024
© The Author(s), under exclusive licence to Springer Science+Business Media, LLC, part of Springer Nature 2024

Abstract

This study aimed to evaluate the production of high purity oxygen (90–95%) through experiments in a PSA/VSA unit and develop a mathematical model to describe the dynamic behavior of the process. Different operational parameters and the dead volume were investigated for their impact on process performance. The experiments used a laboratory-scale unit filled with beads of a commercial LiX zeolite to obtain breakthrough and PSA/VSA data for model validation. Equilibrium isotherms of pure oxygen and nitrogen were measured at 288, 298 and 313 K for the pressure range of 0 to 3 bar. Single and multicomponent breakthrough curves were obtained at 298 K. Synthetic air (grade 5.0 purity, excluding argon) with a composition of 20% ($\pm 0.5\%$) O₂ and 80% ($\pm 0.5\%$) N₂ was used in the PSA/VSA experiments. A novel approach was developed using the mathematical model designed to simulate PSA/VSA cycles to account for the dead volume effects commonly found in units of this type. The model was implemented and solved using gPROMS® software. The simulation data matched well with the experimental data, accurately representing histories of concentration, pressure, temperature, and purity variations during the process. The validated model revealed optimal operating conditions for a VSA unit: 7.5 s adsorption time, 1.5 bar adsorption pressure, 0.1 bar desorption pressure, and a flow rate of 1 SLPM, producing a purity of approximately 94% and a recovery of about 20%. Increasing the adsorption duration negatively affected the oxygen purity but positively influenced process recovery and productivity. Adding an equalization stage improved process recovery by 18.9% for PSA and 14.5% for VSA. Additionally, increased dead volume in the column had adverse effects on purity, productivity, and recovery for both PSA and VSA units.

Keywords Oxygen · Air · Zeolite · PSA · VSA · Simulation

1 Introduction

Oxygen is an essential medicine, needed at all levels of health systems. The use of this gas is necessary for the treatment of a series of diseases, being also a fundamental component for respiratory resuscitation procedures [1, 2]. The large increase in number of COVID-19 infections cases has increased the global demand for this medical supply, since

oxygen therapy had to be administrated for all infected people with severe symptoms [3]. In addition, there was also an increase in the incidence of pneumonia cases, which is one of the main complications associated with cases of COVID-19 infection, putting even more pressure on health systems to increase the demand for oxygen [4].

Although cryogenic distillation is currently the most suitable technology for large-scale production of oxygen with high purity levels [5–7], it is highly energy-intensive. On the other hand, adsorption-based separation processes can be more feasible for small to midscale oxygen production, that is, up to 300 tons of O₂ per day, achieving purities of up to 95% [5, 7–9], which would be sufficient to meet the requirements for medical use.

Air separation by adsorption is often carried out by Pressure Swing Adsorption (PSA) or Vacuum Swinging Adsorption (VSA) operation modes, due to their shorter cycle time

✉ Moisés Bastos-Neto
mbn@ufc.br

¹ Department of Chemical Engineering, Federal University of Ceará, Campus do Pici, Bl. 731, Fortaleza, CE 60760-400, Brazil

² Department of Engineering and Technology, Federal University of the Semi-Arid Region (UFERSA), Mossoró, RN 59625-900, Brazil

and simplified control, in addition to the possibility of being operated under temperature and pressure conditions close to ambient conditions for small-scale production [3, 5, 8, 10]. In recent decades, small-scale PSA-based processes for O₂ production from air have become prominent, with product purity often falling above 90% and modest recovery. On the other hand, VSA-based processes have gained recognition for achieving high O₂ purities offering higher recovery rates in comparison to PSA cycles [5, 11, 12]. Depending on the process conditions, purity requirements and adsorbent efficiency, both operation modes may present energy demands, which can be diminished through the introduction of equalization steps into the operational cycle [12, 13].

Among the available adsorbent materials, zeolites, particularly the lithium-exchanged X-type zeolites (LiX), are recurrently the most suitable for O₂ production from air, due to their high capacity and selectivity for N₂ besides their moderate enthalpy of adsorption [14, 15].

In order to extract the maximum potential of the adsorbent in a given contactor system, a procedure to find the optimal operating conditions is necessary. However, such procedures require processing data, which in turn are generally expensive and very time-consuming. Thus, the use of process modeling and simulation is key for the determination of ideal operating parameters such as cycle time, number of steps, among others. Furthermore, the impact of dead volume in PSA/VSA units at an industrial scale is typically neglected, as the bed volume filled with adsorbent material greatly exceeds the dead volume. However, when working with a bench-scale unit, especially for research purposes, the significance of the dead volume tends to be more pronounced. Overlooking the effects of dead volume in the analysis can result in inadequate model validation or misinterpretation of data. Therefore, the objective of this work is to develop and validate a mathematical model to simulate a VSA unit for the production of high purity O₂ (> 90%) with an evaluation of influence of the adsorption time, desorption pressure, inclusion of equalization steps, and influence of dead volume in process performance.

2 Materials and methods

2.1 Materials

The adsorbent material used was a commercial LiX type zeolite especially developed for air separation, namely Z10-05-03, supplied ZeoChem (Switzerland), with a spherical shape and average particle diameter (d_p) of 1.2 mm. The gases used in the textural characterization as well as in measurement of adsorption isotherms, breakthrough curves and PSA/VSA cycles were helium (99.999%), nitrogen (99.999%), oxygen (99.995%) and synthetic air (99.999%,

excluding argon). The synthetic air was composed of 20% ($\pm 0.5\%$) O₂ and 80% ($\pm 0.5\%$) N₂. All of them supplied by White Martins Praxair Inc. (Brazil).

2.2 Textural characterization

The zeolite was characterized by adsorption–desorption isotherms of N₂ at 77 K with the aid of an Autorsorb iQ₃ equipment (Quantachrome, USA). The specific surface area of the adsorbent material was determined using the BET (Brunauer–Emmett–Teller) method [16, 17]. The micropore volume was evaluated according to the Dubinin–Radushkevich (DR) equation, and the total volume of pores was calculated from the volume adsorbed at $P/P_0 \approx 1$ [16]. The evaluated properties are shown in Table S1 of the Supplementary Material.

2.3 Adsorption isotherms

Adsorption isotherms of pure N₂ and O₂ were measured using a magnetic suspension balance (Rubotherm, Germany) at temperatures of 288, 298 and 313 K in the pressure range of 0–3 bar. The adsorbent sample was previously degassed at 623 K for 12 h under vacuum (10^{-3} bar) to ensure complete removal of any species previously adsorbed. Experiments were carried out with non-adsorbed gas (Helium) to determine the specific volume of solids, which allows to account for the effects of buoyancy in the adsorption measurements. More details about the implemented experimental procedure can be found in the literature [18–20]. The corrections of the values of adsorbed concentration in excess to absolute values were not carried out, since in the pressure range in which the gravimetric tests were carried out, the deviations between the absolute amounts and amounts in excess are negligible [21].

The Extended Langmuir (Eq. 1) model was used to describe mixed gas adsorption behavior, in order to account for the competitive adsorption effects of different species. This model uses the parameters obtained from the fittings for the isotherms of each component (i, j) and maintains the same assumptions of the classic single-component Langmuir model [22].

$$q_i^* = \frac{q_{max,i} b_i P_i}{1 + \sum_{j=1}^n b_j P_j} \quad (1)$$

where q_{max} is the theoretical maximum adsorption capacity, b is the adsorbent-adsorbate affinity coefficient and P is the equilibrium pressure. The affinity parameter (b) was described as a function of temperature, in order to consider the thermal effects during the adsorption process as shown in Eq. 2.

$$b_i = b_{\infty,i} \exp\left(\frac{Q_i}{RT_g}\right) \tag{2}$$

where b_{∞} is the Langmuir affinity constant at the reference temperature and Q is the enthalpy of adsorption from the Langmuir equation, R is the ideal gas constant, and T_g is the gas phase temperature.

2.4 Column dynamics

Breakthrough curves and PSA/VSA operation data were measured in a dual-bed PSA unit—PSA-1000 (L&C Science and Technology, USA), as described and used in previous studies [23]. The composition of the gas mixture was set with the aid of volumetric flow controllers (Parker, USA) and measured at the bed outlet with a 580 Series gas chromatograph (Gow-Mac Instruments Co., USA). The temperature inside each column is monitored by thermocouples axially distributed (0.150 m, 0.275 m, 0.400 m and 0.525 m). The properties of the column and bed are summarized in Table S2 of the Supplementary Material.

Prior to each test, the column was heated to about 623 K, under vacuum (10^{-3} bar), for about 12 h, in order to ensure a complete degasification of the adsorbent material. The column was then subjected to a flow of He until the pressure and temperature conditions previously established for each experiment were reached. The determination of the adsorbed amount of each component was performed as described in Wilkins et al. [24]. Table 1 summarizes the operating conditions used in the measurements and simulations of breakthrough curves.

2.5 PSA/VSA cycles

The PSA and VSA cycles consisted of six steps each: pressurization, adsorption, equalization-depressurization

(eq-depr), blowdown, purge and equalization-pressurization (eq-press). The schedule of both operation modes including the duration of each step is shown in Table 2.

Before each experimental run, both beds were regenerated according to the procedure described in the previous section. For the VSA operation, the following conditions were applied: adsorption time of 7.5 s; adsorption pressure of 1.5 bar; blowdown step was carried out under vacuum; and the equalization steps lasted 2 s. The PSA operating mode was carried out with the following conditions: adsorption time of 15 s; adsorption pressure of 2.5 bar; a lower pressure of 1 bar (instead of vacuum); and equalization steps of 2 s. The duration of the equalization step was determined experimentally, relying on the pressure difference between the two columns. The cycle advances once the difference reaches the predefined tolerance value in the control unit. The observed time averaged approximately 2 s. In the purge step, a stream equivalent to 2% of the high-purity product was employed. For both operation modes, the feed rate was 1 SLPM.

To evaluate the influence of equalization steps and desorption pressure in the VSA operation, simulations were conducted using an adsorption time of 15 s for both operations, which is an average value within the analyzed interval. As for the analysis of the influence the dead volume, the adsorption times implemented in the experiment (as shown in Table 2) were used to enable a comparison of the purity data with those observed in the experimental unit with a dead volume of 43%.

2.5.1 Mathematical model

The mathematical model used to describe the dynamic behavior of gas separation in a fixed bed (refer to the Supplementary Material) has been validated and reported in previous studies [3, 9, 12, 25–27]. However, some modifications regarding the description of thermal effects, pressure

Table 1 Operating conditions for the measurement of breakthrough curves

Binary mixture	Ratio	Pressure (bar)	Volumetric flowrate
N ₂ + O ₂ (in He)	79:21	2.3	2.6 SLPM
Single component	Composition	Pressure (bar)	Volumetric flowrate
N ₂ (in He)	14%	2.1	2.7 SLPM
O ₂ (in He)	14%	2.7	2.6 SLPM

Table 2 Implemented schedule of the PSA and VSA cycles

	PSA	VSA	Column 1	Column 2			
t_{PR}	40 s		Pressurization	Blowdown			
t_{AD}	15 s	7.5 s	Adsorption	Purge			
t_{EQ}	2 s	2 s	eq-depr	eq-press			
t_{BL}	40 s	120 s	Blowdown	Pressurization			
t_{PU}	15 s	7.5 s	Purge	Adsorption			
t_{EQ}	2 s	2 s	eq-press	eq-depr			

drop and equilibrium models have been made in this work as described in “[Adsorption isotherms](#)” and “[Accounting the dead volume](#)”. The following assumptions and simplifications were made: the gas phase behaves as an ideal gas along the column; gradients of mass, energy and momentum are considered only in the axial (z) direction; mass transfer resistance is described by the linear driving force (LDF) approximation model, with the mass transfer coefficient (K_{LDF}) estimated from the experimental breakthrough data; thermal equilibrium between the gas and solid phases; enthalpies of adsorption and heat transfer coefficient constant are temperature-independent; the adsorbent is homogeneously packed in the column, resulting in a constant bed porosity; Ergun's equation is valid locally, considering only the terms of pressure drop and velocity in the moment balance [3, 9, 12, 24–28].

The isosteric enthalpy of adsorption was evaluated from the single-component adsorption isotherms obtained at three different temperatures using the Clausius–Clapeyron equation [16, 29] (Eq. 3).

$$\Delta H^{iso} = R \left(\frac{\partial}{\partial \left(\frac{1}{T_g} \right)} \ln(P) \right)_q \quad (3)$$

Table 3 lists the assumed boundary and initial conditions for the simulation of breakthrough curves. The nomenclature for the following parameters is provided in the Supplementary Material.

The mathematical model used to simulate the PSA/VSA processes is essentially the same used for describing breakthrough curves, but with changing boundary conditions,

which will depend on each stage of the cycle. The initial conditions of each step are the final conditions of the previous operating step. For the equalization stage, it was assumed that the equilibrium pressure is equal to the arithmetic mean of the pressures of the two columns. The boundary conditions used for PSA/VSA simulations are shown in Table 4. Tables S3–S5 in the Supplementary Material provide a summary of the primary correlations used for solving the model. Furthermore, Table S6 presents the parameter values used in the model's equations.

P_{EQ} is the equilibrium pressure in the end of equalization step. The molar flow rate in equalization-pressurization ($F_{i_{EQd}}$) denotes the ratio of the amount of component i that leaves the other column during the equalization-depressurization step.

The performance parameters used to evaluate the PSA/VSA processes (product purity, recovery and productivity) were calculated according to Eqs. 4–6.

$$Purity = \frac{\sum_{AD} \left(\int_0^{t_{AD}} F_{O_2,out} dt \right)}{\sum_{AD} \left(\int_0^{t_{AD}} F_{O_2,out} dt + \int_0^{t_{AD}} F_{N_2,out} dt \right)} \quad (4)$$

$$Recovery = \frac{\sum_{AD} \left(\int_0^{t_{AD}} F_{O_2,out} dt \right) - \sum_{PU} \left(\int_0^{t_{PU}} F_{O_2,in} dt \right)}{\sum_{AD} \left(\int_0^{t_{AD}} F_{O_2,in} dt \right) + \sum_{PR} \left(\int_0^{t_{PR}} F_{O_2,in} dt \right)} \quad (5)$$

$$Productivity = \frac{\sum_{AD} \left(\int_0^{t_{AD}} F_{O_2,out} dt \right) - \sum_{PU} \left(\int_0^{t_{PU}} F_{O_2,out} dt \right) - \sum_{PR} \left(\int_0^{t_{PR}} F_{O_2,in} dt \right)}{mass\ of\ dry\ adsorbent\ t_{ciclo}} n_{beds} \quad (6)$$

Table 3 Initial and boundary conditions for the simulation of breakthrough curves

$t=0$	
$y_i = 0$	
$T_g = T_w = 298K$	
$\frac{\partial \bar{q}_i}{\partial t} = 0$	
$C_{g,T} = C_{g,T0}$	
$z=0$	$z=L$
$\dot{V}_{inlet}^0 \left(\frac{P^0}{RT^0} \right) \frac{1}{A} = (u C_{g,T}) \Big _0$	$\frac{\partial C_{g,T}}{\partial z} \Big _L = 0$
Total amount of gas in molar basis at the inlet and outlet of the column	
$\dot{V}_{inlet}^0 \left(\frac{P^0}{RT^0} \right) \frac{y_{i0}}{A} = (u C_{g,i}) \Big _0 - D_{ax,i} \frac{\partial C_{g,i}}{\partial z} \Big _0$	$\frac{\partial C_{g,i}}{\partial z} \Big _L = 0$
Amount of component i in molar basis entering and its variation at the column outlet	
Pressure of the system at the outlet	
$\dot{V}_{inlet}^0 \left(\frac{P^0}{RT^0} \right) \frac{1}{A} c_{p,g} T_0 = (u C_{g,T} c_{p,g} T_g) \Big _0 - \lambda \frac{\partial T_g}{\partial z} \Big _0$	$P _L = P_{exp}$ $\frac{\partial T_g}{\partial z} \Big _L = 0$
Amount of energy of the gas stream that entering and leaving the column	

Table 4 Boundary conditions used in the simulation of PSA/VSA processes

$z = 0$	$z = L$
<i>Pressurization</i>	
$\dot{V}_{inlet}^0 \left(\frac{P^0}{RT^0} \right) \frac{y_{i,0}}{A} = (uC_{g,i}) _0 - D_{ax,i} \frac{\partial C_{g,i}}{\partial z} \Big _0$	$\frac{\partial C_{g,i}}{\partial z} \Big _L = 0$
$\dot{V}_{inlet}^0 \left(\frac{P^0}{RT^0} \right) \frac{1}{A} = u _0$	$u _L = 0$
$\dot{V}_{inlet}^0 \left(\frac{P^0}{RT^0} \right) \frac{1}{A} c_{p,g} T_0 = (uC_{g,T} c_{p,g} T_g) _0 - \lambda \frac{\partial T_g}{\partial z} \Big _0$	$\frac{\partial T_g}{\partial z} \Big _L = 0$
$\frac{\partial T_w}{\partial z} \Big _0 = 0$	$\frac{\partial T_w}{\partial z} \Big _L = 0$
<i>Adsorption</i>	
$\dot{V}_{inlet}^0 \left(\frac{P^0}{RT^0} \right) \frac{y_{i,0}}{A} = (uC_{g,i}) _0 - D_{ax,i} \frac{\partial C_{g,i}}{\partial z} \Big _0$	$\frac{\partial C_{g,i}}{\partial z} \Big _L = 0$
$\dot{V}_{inlet}^0 \left(\frac{P^0}{RT^0} \right) \frac{1}{A} = u _0$	$\frac{\partial P}{\partial t} \Big _L = 0$
$\dot{V}_{inlet}^0 \left(\frac{P^0}{RT^0} \right) \frac{1}{A} c_{p,g} T_0 = (uC_{g,T} c_{p,g} T_g) _0 - \lambda \frac{\partial T_g}{\partial z} \Big _0$	$\frac{\partial T_g}{\partial z} \Big _L = 0$
$\frac{\partial T_w}{\partial z} \Big _0 = 0$	$\frac{\partial T_w}{\partial z} \Big _L = 0$
<i>Blowdown</i>	
$\frac{\partial C_{g,i}}{\partial z} \Big _0 = 0$	$\frac{\partial C_{g,i}}{\partial z} \Big _L = 0$
$P _0 = (P_{AD} - P_{PU}) \exp(0.2t) + P_{PU}$	$u _L = 0$
$\frac{\partial T_g}{\partial z} \Big _0 = 0$	$\frac{\partial T_g}{\partial z} \Big _L = 0$
$\frac{\partial T_w}{\partial z} \Big _0 = 0$	$\frac{\partial T_w}{\partial z} \Big _L = 0$
<i>Purge</i>	
$\frac{\partial C_{g,i}}{\partial z} \Big _0 = 0$	$-\dot{V}_{PU,inlet}^0 \left(\frac{P^0}{RT^0} \right) \frac{y_{PU,i,0}}{A} = (uC_{g,i}) _0 - D_{ax,i} \frac{\partial C_{g,i}}{\partial z} \Big _0$
$\frac{\partial P}{\partial t} \Big _0 = 0$	$-\dot{V}_{inlet}^0 \left(\frac{P^0}{RT^0} \right) \frac{1}{A} = u _L$
$\frac{\partial T_g}{\partial z} \Big _0 = 0$	$\frac{\partial T_g}{\partial z} \Big _L = 0$
$\frac{\partial T_w}{\partial z} \Big _0 = 0$	$\frac{\partial T_w}{\partial z} \Big _L = 0$
<i>Equalization-depressurization</i>	
$\frac{\partial C_{g,i}}{\partial z} \Big _0 = 0$	$\frac{\partial C_{g,i}}{\partial z} \Big _L = 0$
$u _0 = 0$	$P _L = (P - P_{EQ}) \exp(0.2t) + P_{EQ}$
$\frac{\partial T_g}{\partial z} \Big _0 = 0$	$\frac{\partial T_g}{\partial z} \Big _L = 0$
$\frac{\partial T_w}{\partial z} \Big _0 = 0$	$\frac{\partial T_w}{\partial z} \Big _L = 0$
<i>Equalization-pressurization</i>	
$\frac{\partial C_{g,i}}{\partial z} \Big _0 = 0$	$-F_{i_{EQ}^d} \frac{1}{A} = (uC_{g,i}) _L - D_{ax,i} \frac{\partial C_{g,i}}{\partial z} \Big _L$
$u _0 = 0$	$-\sum F_{i_{EQ}^d} \frac{1}{A} = (uC_{g,T}) _L$
$\frac{\partial T_g}{\partial z} \Big _0 = 0$	$-\sum F_{i_{EQ}^d} \frac{1}{A} c_{p,g} T_0 = (uC_{g,T} c_{p,g} T_g) _0 - \lambda \frac{\partial T_g}{\partial z} \Big _L$
$\frac{\partial T_w}{\partial z} \Big _0 = 0$	$\frac{\partial T_w}{\partial z} \Big _L = 0$

where F is the molar flow rate of component i , n_{beds} represents the number of beds (2) and t represents the time of each step (AD: Adsorption; PU: Purge; PR: Pressurization).

The system of partial differential equations was solved with gPROMS (Process System Enterprise, UK). The numerical method applied to discretize the axial domain was the third-order orthogonal collocation of finite elements

(OCFEM), applied on 15 finite elements. The absolute error tolerance was 1×10^{-5} .

The proposed mathematical model was validated by comparing simulation results with data obtained experimentally from: breakthrough curves; pressure and temperature histories as well as from purity data for PSA and VSA operations.

2.5.2 Accounting the dead volume

The column length (0.955 m) presented in Table S1 represents the total length of the column, taking into account both the space filled by the adsorbent material and the space corresponding to the valves, tubes and filters used in the unit. The length of the column filled with the adsorbent material, i.e., the bed length, was 0.549 m and was the same for all experiments. Thus, the space not filled by adsorbent material (dead volume) represents about 43% of the total volume and has been considered in the modeling. In many studies, the impact of this volume is often disregarded, as the fraction filled with adsorbent material significantly outweighs the remaining dead volume, justifying its neglect. However, in the case of this study, considering such effects was imperative, due the fact that the used bench-scale PSA/VSA unit column featured additional components, such as supports, filters, and other elements, which, given the scale, exhibited proportionally larger dimensions.

Furthermore, to enhance material regeneration, the heaters responsible for heating the bed were strategically positioned closer to the column's center. As a result, the bed volume was reduced to ensure complete coverage by the heaters, leading to a significant increase in dead volume. This substantial alteration justified the need to account for the effects stemming from this aspect.

Since there is no adsorbent material in the dead volume, some terms of the model equations corresponding to this volume are null. In this way, the mass, energy and momentum balances for the dead volume sections are presented as follows, respectively.

$$\frac{\partial}{\partial z} \left(\varepsilon D_{ax,i} C_{g,T} \frac{\partial y_i}{\partial z} \right) - \frac{\partial}{\partial z} (u C_{g,i}) - \frac{\partial C_{g,i}}{\partial t} = 0 \quad (7)$$

$$\frac{\partial}{\partial z} \left(\lambda \frac{\partial T_g}{\partial z} \right) - u C_{g,T} \tilde{c}_{p,g} \frac{\partial T_g}{\partial z} + RT_g \frac{\partial C_{g,T}}{\partial t} - 4 \frac{h_w}{d_i} (T_g - T_w) = 0 \quad (8)$$

$$-\frac{\partial P}{\partial z} = \delta u \quad (9)$$

The pressure drop in the dead volume was considered negligible, therefore, the δ coefficient was chosen so that the pressure drop is practically zero. All other parameters and boundary conditions remain the same as presented in the previous section.

For the analysis of the influence of this variable on the performance of the project through simulations, the dead volume sections were defined as having the same dimension at the top and at the end of the column.

2.6 Model parameters

The correlations used to obtain the bed, particle, mass transfer, energy transfer and momentum transfer parameters and the corresponding applied values are presented in the Supplementary Material. Details regarding the correlations can be found elsewhere [30–32]. The axial mass dispersion coefficient of the mixture was calculated from the coefficients of the pure components, the feeding molar fractions and a series of dimensionless numbers. The binary diffusivity for each pair in the mixtures O₂/He, N₂/He and O₂/N₂ was also obtained from the procedure described in the literature [33].

The axial heat dispersion coefficient was obtained from a correlation with the thermal conductivity of the gas mixture, which was calculated from the thermal conductivity of each gas in the feeding conditions. The thermal conductivity of the wall was obtained from the literature [30–32, 34]. The viscosity of the mixture was calculated by the Wilke equation and the density of the gas mixture was calculated by the ideal gas law [35].

3 Results

3.1 Adsorption isotherms

The isotherms of pure N₂ and O₂ for the Z10-03-05 zeolite sample are shown in Fig. 1. The Langmuir model satisfactorily fits to the experimental data. As evidenced by the results, this particular adsorbent has an increased preferential adsorption of nitrogen, allowing for the equilibrium

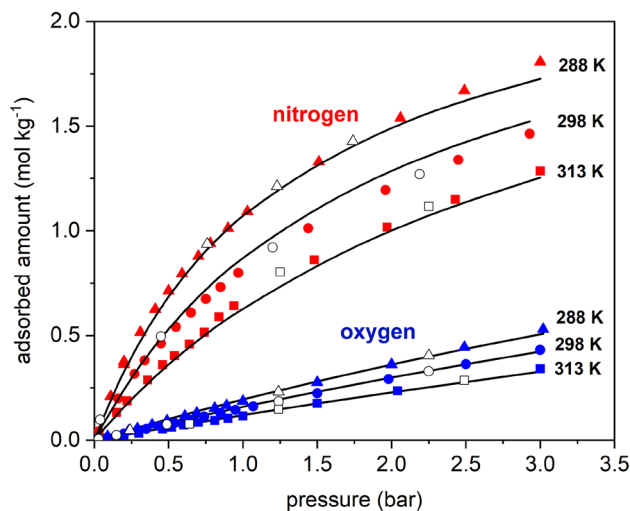


Fig. 1 Adsorption isotherms of N₂ and O₂ on Z10-03-05 at temperatures of 288, 298 and 313 K (symbols) and Langmuir fit (lines). Filled symbols represent the adsorption branch and open symbols the desorption branch of the experimental isotherms

Table 5 Model parameters of Langmuir equation for N₂ and O₂ adsorption equilibrium isotherms

Adsorbate	$q_{max,i}$ (mol kg ⁻¹)	$b_{\infty,i}$ (bar ⁻¹)	Q_i (kJ mol ⁻¹)	R^2 (-)	ΔH_i^{iso} (kJ mol ⁻¹)
N ₂	2.48	3.1×10^{-5}	24.2	0.994	-23.4
O ₂	2.48	1.2×10^{-4}	15.6	0.998	-14.2

selective separation of air, which leaves oxygen as the raffinate product. Similar results for the adsorption equilibrium of both oxygen and nitrogen have been reported in the literature [36, 37].

For comparison purposes, at a pressure of approximately 1.5 bar, which is the adsorption pressure under VSA operation mode, the adsorbed amounts of N₂ and O₂ are 1.01 and 0.22 mol kg⁻¹, respectively. The preference for N₂ over O₂ is associated to the interactions between the electrostatic field of the cationic zeolite and the quadrupole moment of the N₂ and O₂ molecules, with the quadrupole moment of N₂ being about three times greater than that of O₂ [14, 38]. This difference leads to a stronger interaction of nitrogen molecules with lithium cations present in the zeolite structure, favoring a selective adsorption of N₂ molecules on the surface of the material [3, 37, 39, 40].

The parameters of the Langmuir equation and the isosteric enthalpy of adsorption are summarized in Table 5. As expected, both parameters related to the enthalpy of adsorption, Q and $\Delta H_{O_2}^{iso}$, presented higher values for N₂ compared to O₂, indicating preferential adsorption for the first. Similar results are reported by Rege and Yang [15] for the isosteric enthalpy of adsorption of N₂ and O₂ on a LiX zeolite, with values of 23.4 and 13.2 kJ mol⁻¹ for N₂ and O₂, respectively.

The overlapping of adsorption and desorption data evidences no hysteresis and complete reversibility under such conditions, which is a desirable feature for adsorptive cyclic processes.

3.2 Column dynamics

3.2.1 Single component curves

The obtained experimental and simulated breakthrough curves are shown in Fig. 2. The model was able to describe the experimental data satisfactorily, with minor deviations in the region close to saturation, which are generally related to heat effects and temperature dispersion inside the bed. The differences observed for the adsorbed amounts from the experimental and simulated data were around 8% for N₂ and 10% for O₂.

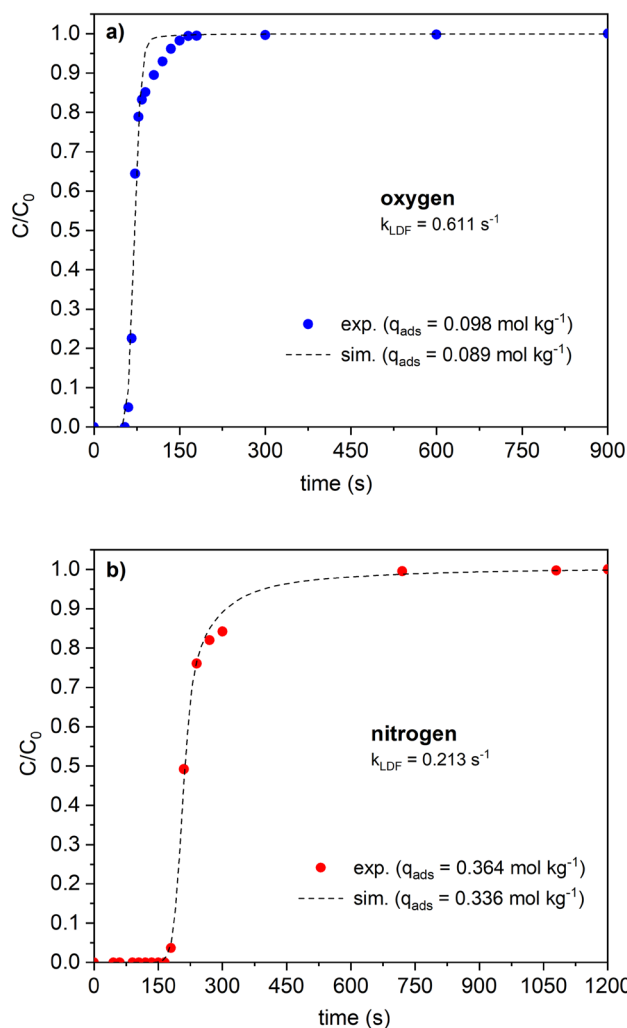


Fig. 2 Comparison between the breakthrough curves obtained experimentally and those obtained through the model for O₂ (a) and N₂ (b). Symbols denote experimental data, while the dashed line represents the simulation

In order to verify the accuracy of the column dynamics measurements, the adsorbed amounts calculated from the breakthrough curves were compared to the isotherms of both gases at 298 K, as shown in Fig. 3. A good match is observed despite the minor deviation of the adsorbed amount for O₂. The slight discrepancy observed may be attributed to the errors inherent in the two experimental methods used. It has been reported that dynamic methods may yield data with an error margin of approximately 10%, whereas static methods tend to produce data with errors below 5% [33].

The lumped mass transfer coefficient, K_{LDF} , for each gas was estimated as a fitting parameter of the model to the experimental breakthrough curves. The values obtained were 0.611 s⁻¹ for O₂ and 0.213 s⁻¹ for N₂. Similar values were reported by Jee et al. [12], with 0.62 and 0.197 s⁻¹ for O₂ and N₂, respectively, using a 13X zeolite as adsorbent.

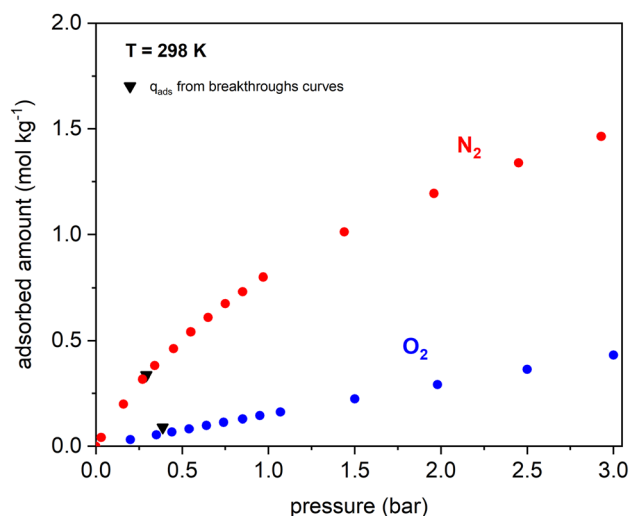


Fig. 3 Comparison between the adsorbed amounts obtained from the breakthrough curves and the equilibrium isotherms by gravimetry

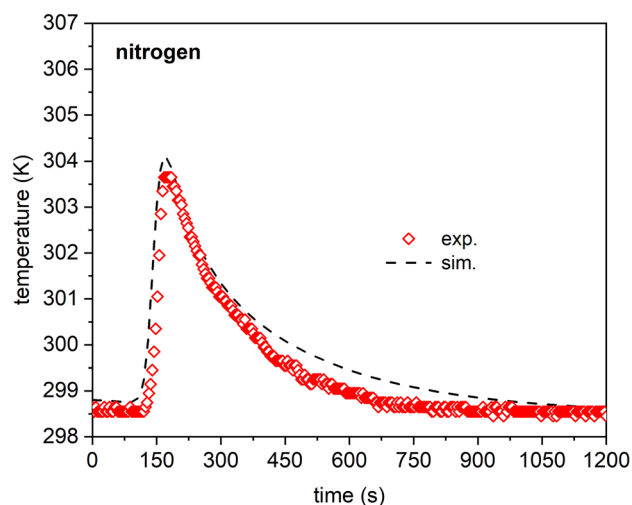


Fig. 5 Temperature variation close to the bed outlet for the N_2 experiment. Symbols denote experimental data, while the dashed line represents the simulation

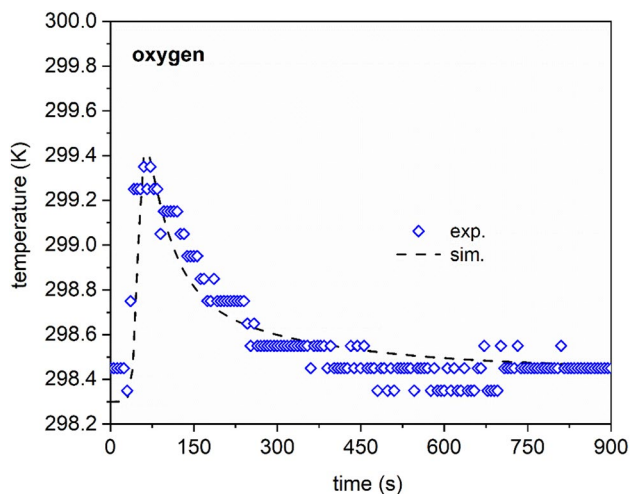


Fig. 4 Temperature variation close to the bed outlet for the O_2 experiment. Symbols denote experimental data, while the dashed line represents the simulation

A similar behavior, where O_2 presented K_{LDF} values about 3–4 times higher than N_2 , was also observed in other types of zeolites [41].

The temperature variation recorded by the thermocouple closest to the bed outlet during the experiments with each gas is shown in Figs. 4 and 5. Temperature has increased roughly 1 and 5 K during the experiments with oxygen and nitrogen, respectively. A good agreement between experimental and simulated data, not only for the breakthrough time but also for the peak height (maximal temperature reached) and peak width (conversion and dispersion phenomena), can be observed for both gases. The preferential

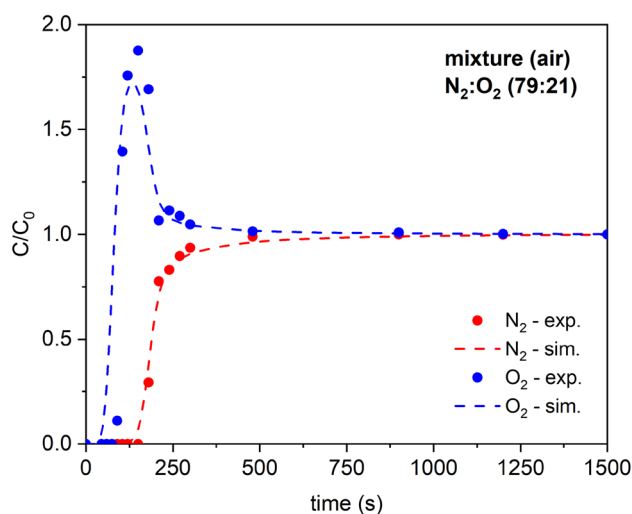


Fig. 6 Comparison between the experimentally obtained multicomponent breakthrough curves and those obtained through the model for the N_2/O_2 mixture. Symbols denote experimental data, while the dashed lines represent the simulation

adsorption for N_2 related to the higher enthalpy of adsorption explains the higher temperature increase.

3.2.2 Multicomponent curves

The experimental and simulated multicomponent breakthrough curves are shown in Fig. 6. Although a slight discrepancy is observed for oxygen in the roll-up and breakthrough time, the model was able to describe the general behavior satisfactorily.

The typical shape of multicomponent breakthrough curves indicates the competition for adsorption sites with the displacement of the less adsorbed component —oxygen— by the preferentially adsorbed one—nitrogen. The resulting overshoot in the concentration history occurs due the slower movement of the concentration front of N_2 in comparison with the concentration front of the less adsorbed component (O_2) [24].

Figure 7 presents the experimental results of temperature history close to the bed outlet compared with the simulated data. Two temperature peaks are detected, each one associated to the heat generated by the adsorption of O_2 and N_2 , respectively. It was also possible to observe that there is a satisfactory match between the simulated and experimental data.

3.3 Model validation for cyclic separation

Experimental and simulated pressure histories for a cyclic operation are shown in Fig. 8. The comparison is made after approximately 2 h from the beginning of the experimental run to ensure that the cyclic steady-state (CSS) has been reached. The duration of each stage and progression of pressure during the cycle is well represented by the mathematical model, confirming its suitability to describe the operation of a PSA unit.

In order to validate the PSA model, the experimentally achieved O_2 purity, calculated from the outlet gas composition, was compared to the purity estimated by simulation. The data were extracted during the adsorption step (ADS) at approximately 5, 10 and 15 s and averaged for different cycles of an operation at CCS. The obtained results are shown in Fig. 9, with deviations ranging from 3–8%,

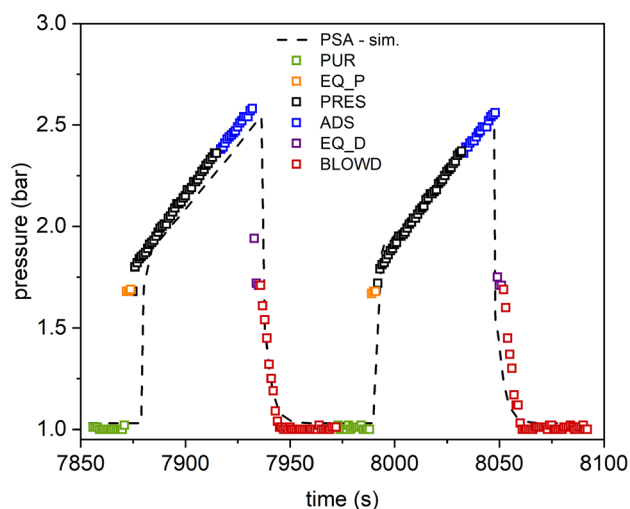


Fig. 8 Operating pressure throughout the PSA cycle. Symbols denote experimental data, while the dashed line represents the simulation

which is satisfactorily, considering the high complexity of this cyclic dynamic operation. It is noteworthy that the synthetic air used in these experiments had a purity of 99.999%, excluding argon (Ar). As a result, the presence of argon in the synthetic air is at trace levels (less than 0.001%), exerting a negligible influence on the results.

An experimental run for VSA mode was also carried out in order to evaluate the accuracy of the model in predicting the O_2 purity under such operating conditions. The model predicted an O_2 purity of approximately 92%, whereas the experimentally observed purity was approximately 94%. Considering the limitations of the unit in operating at vacuum range, the discrepancy was even lower than that

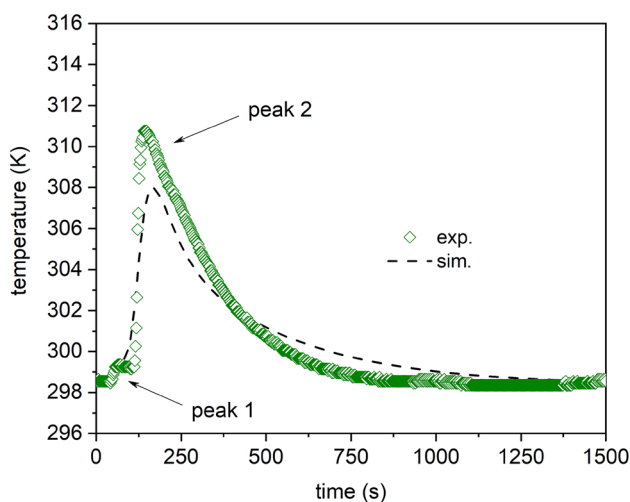


Fig. 7 Temperature variation close to the outlet for the multicomponent experiment. Symbols denote experimental data, while the dashed line represents the simulation

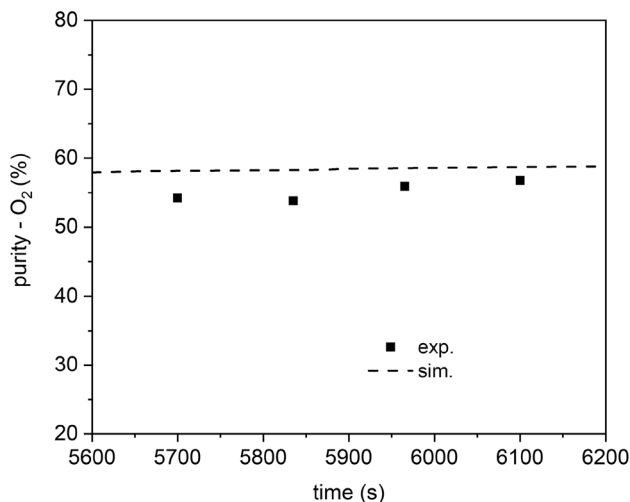


Fig. 9 Oxygen purity data for model validation for a PSA operation at cyclic steady-state. The experimental data correspond to the PSA cycles 50 through 53

found for the PSA operation, with a good agreement between estimated and measured values.

3.4 Air separation performance under PSA/VSA modes

After the validation procedure, the proposed model (PSA/VSA) was used in a parametric analysis in order to explore different operating conditions, verify the impact of the set steps and assess the unit's performance. The outcomes and insights derived from simulations using the previously validated model are presented in the subsequent subsections.

3.4.1 PSA/VSA adsorption time

The influence of the adsorption time on the purity and recovery of O_2 achieved by PSA and VSA operations has been investigated. All other parameters for the other steps were kept the same as described in Table 2. The first was to use the model to determine the concentration profile of N_2 in the gas phase inside the column. The adsorption time ranged from 5–30 s and the results for PSA and VSA are shown in Figs. 10 and 11, respectively.

One should bear in mind that the initial and final approximately 0.2 m of the column length correspond to the dead volume. Due to the absence of adsorbent material in these sections, there is no adsorption taking place and, consequently, the N_2 concentration remains constant, as observed in Fig. 11. As soon as the gas mixture comes into contact with the adsorbent material, N_2 fraction in the gas phase decreases due to its adsorption. The longer the adsorption step occurs, the more the concentration front moves along the bed as the material begins to get saturated. For this reason, faster adsorption steps lead to the lower N_2 fraction at

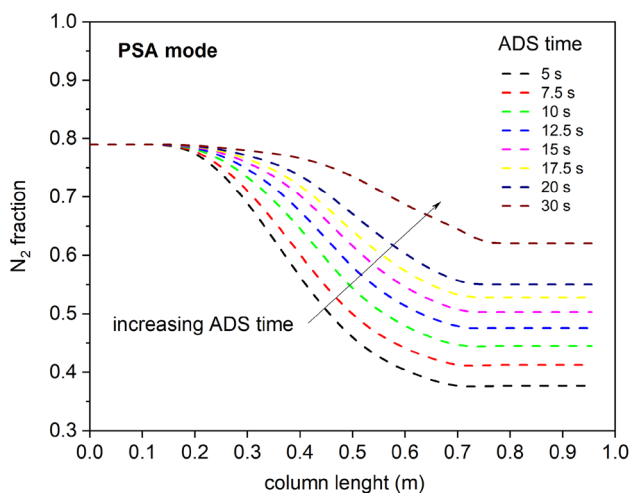


Fig. 10 Fraction of N_2 along the column for different adsorption times

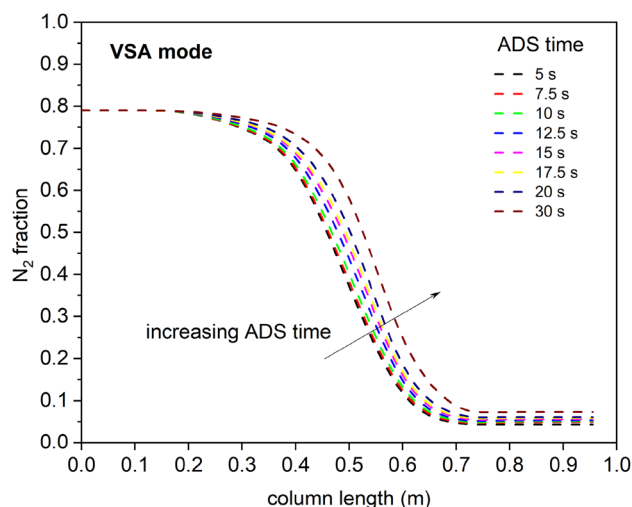


Fig. 11 Fraction of N_2 along the column for different adsorption times

the end of the bed and consequently higher purities, independently of the operation mode. On the other hand, as the nitrogen front advances through the bed, more oxygen is displaced by competitive adsorption (see Fig. 6) and released to the gas phase as part of the product stream before the end of the adsorption step. If not displaced by nitrogen, the adsorbed oxygen molecules would be purged in a following step and would not be accounted in the product stream. As a consequence, the product (O_2) recovery and productivity present a behavior inverse to that of the purity with respect to the adsorption time. The decision for the most suitable adsorption time should take this trade-off carefully into account. The resulting O_2 purity, recovery and productivity for PSA and VSA operation modes are presented in Figs. 12 and 13.

For the PSA mode, the productivity obtained for the adsorption time of 15 s was $33.9 \text{ g h}^{-1} \text{ kg}_{\text{ads}}^{-1}$, while for 5 and 30 s it was 13.74 and $48.34 \text{ g h}^{-1} \text{ kg}_{\text{ads}}^{-1}$, respectively. In the case of the VSA operation, for an adsorption time of 15 s a productivity of $19.4 \text{ g h}^{-1} \text{ kg}_{\text{ads}}^{-1}$ was reached, whereas for the adsorption times of 5 and 30 s the observed productivity was 6.30 and $33.58 \text{ g h}^{-1} \text{ kg}_{\text{ads}}^{-1}$, respectively. Similar behavior regarding the influence of the duration of the adsorption step on these parameters were observed by Rao [42] for the PSA operation. As for the VSA operation, a similar behavior was observed by Jee [12, 42].

Comparing the influence of the adsorption time among both operation modes, it is possible to conclude that they are analogous. However, the sensitivity presented by the VSA operation was lower, with narrower N_2 concentration profiles in the gas phase for the different adsorption times. This phenomenon can be explained by the more effective regeneration of the adsorbent provided by the use of vacuum

Table 7 Influence of desorption pressure on pressurization time, recovery, productivity and purity of the product obtained in the VSA process

Desorption pressure (bar)	Pressurization time (s)	Purity—O ₂ (%)	Recovery—O ₂ (%)	Productivity (g h ⁻¹ kg _{ads} ⁻¹)
0.1	120	91.23	20.39	19.4
0.2	105	85.78	22.52	21.4
0.3	87	79.27	25.67	24.32
0.4	71	71.7	29.21	27.58
0.5	56	63.04	33.4	31.37

since there is a decrease in the range of variation between adsorption–desorption pressure, causing part of the N₂ adsorbed in the adsorption step to remain retained in the column during the desorption step. This effect reduces the work capacity of the adsorbent, allowing the N₂ adsorption front to advance further along the bed, leading to product contamination (i.e., less purity).

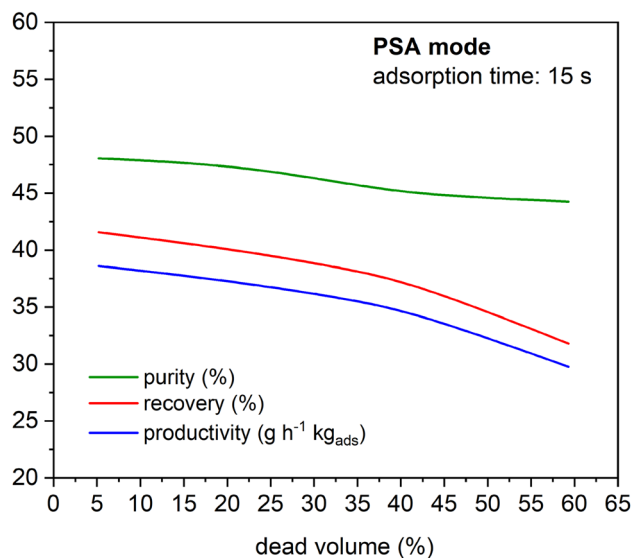
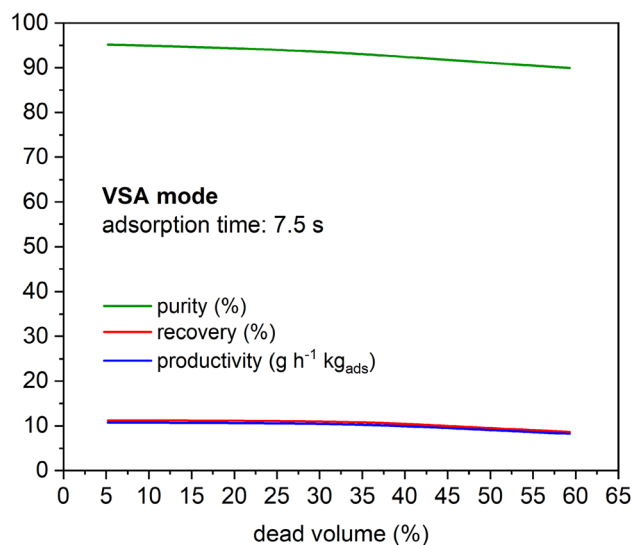
The impact on productivity and recovery was the opposite: increasing the desorption pressure led to higher levels of productivity and recovery in the process. This effect is due to the reduced loss of O₂ during the desorption step, as some of this gas that would otherwise be lost is purged from the column and added to the product stream because of the greater advancement of the N₂ front. Moreover, the reduction in the time required for column pressurization also has a positive effect on productivity and recovery since a smaller amount of gas is fed into the column. This positive effect can be observed through the equations presented in “[Mathematical model](#)”.

3.4.4 Influence of dead volume in PSA/VSA processes

Similarly, the effect of fraction of dead volume has been evaluated for both operation modes, keeping the other conditions unchanged. As previously detailed, the adsorption time was 15 s for PSA operation and 7.5 s for VSA operation. The results are shown in Fig. 14 (PSA) and Fig. 15 (VSA).

In both operation modes, an increase in the fraction of dead volume in the system leads to a reduction in performance parameters. This is because a larger amount of gas must be fed into the column to fill the additional space, which prolongs the pressurization step and increases the total cycle time, even when the feed flow is constant. Furthermore, during the blowdown and purge steps, some of the excess gas fed during the adsorption step is lost, which further diminishes productivity and recovery. This effect has been documented in the literature [8].

The decrease in the O₂ purity with increasing fraction of dead volume may be associated with two main factors. First, the duration of the purge step in the adopted process is associated with the duration of the adsorption step and was kept unchanged for the simulations performed. Since there is an increase in dead volume, part of the gas

**Fig. 14** Influence of the dead volume fraction in a PSA process on Productivity; Recovery and Purity**Fig. 15** Influence of the dead volume fraction in a VSA process on Productivity; Recovery and Purity

fed during the purge step is used to fill the space without adsorbent, causing a less efficient purge to occur. Thus, the greater the dead volume, the less efficient the purge step will be, negatively affecting the purity of the process. In addition, the duration of the adsorption step was kept constant, however, the duration of the pressurization step is increased with increasing dead volume, causing the adsorption front to advance further along the column, also negatively affecting the purity. The results for the VSA process are shown below:

The trends observed for the PSA operation were also observed for the VSA operation. A comparison of the purities obtained for a column operating with 5% and 60% dead volume showed a reduction of 7.9 and 5.5% for the PSA and VSA operations, respectively. This difference can be explained by the application of vacuum during the desorption step in the VSA process, which tends to reduce the negative effect of the less efficient purge for the greater presence of dead volume.

4 Conclusions

This work presented a mathematical model for simulating an adsorption-based separation process to produce oxygen from an air mixture containing mainly nitrogen and oxygen. Both PSA and VSA operating modes were analyzed. The study demonstrated that the commercial zeolite (Z10-05-03) was a suitable adsorbent for the separation of O₂ from N₂/O₂ mixtures, where nitrogen was preferentially adsorbed at low pressures. The proposed model was able to predict the dynamics of single and multicomponent adsorption, validate experimental data for the PSA operation, and allow for the evaluation of different operational parameters. It also demonstrated that obtaining high purities and viable processes while maintaining productivity and recovery was challenging.

The validated model facilitated the determination of the operational conditions of the VSA process necessary to achieve the goal of producing O₂ with purities greater than 90%. These conditions were subsequently implemented in the operation of the unit, resulting in an experimental O₂ purity of about 94%. This highlights the importance of considering the destination of the oxygen obtained at the end of the process, given that different applications may require different levels of purity. By making the conditions implemented more flexible, higher recoveries and productivity can be achieved when the required O₂ purity does not have to be as high. Overall, the proposed model provided a comprehensive understanding of the separation process and can be used to optimize operational conditions, inform future designs, and guide industrial applications.

Supplementary Information The online version contains supplementary material available at <https://doi.org/10.1007/s10450-024-00443-0>.

Acknowledgements The authors acknowledge the support from Fundação Cearense de Apoio ao Desenvolvimento Científico e Tecnológico (FUNCAP), Coordenação de Aperfeiçoamento de Pessoal de Nível Superior (CAPES) and Conselho Nacional de Desenvolvimento Científico e Tecnológico (CNPq).

Author contributions All authors contributed to conception and design of the study. GJAH performed all experiments under supervision of AEBT and MBN. GJAH, AEBT and RBR developed the mathematical model. GJAH and RBR wrote the first draft of the manuscript. RBR and MBN revised, edited and provided a formal analysis of the manuscript. DCSA and MBN acquired and provided funds for the development of this work. All authors approved the submitted version.

Funding This work has been financially supported by: Fundação Cearense de Apoio ao Desenvolvimento Científico e Tecnológico (FUNCAP) Coordenação de Aperfeiçoamento de Pessoal de Nível Superior (CAPES) Conselho Nacional de Desenvolvimento Científico e Tecnológico (CNPq).

Data availability Data will be made available upon request.

Declarations

Conflict of interests The authors declare no conflict of interest.

Ethical approval Not applicable.

References

1. Organization, W.H.: Technical specifications for pressure swing adsorption (PSA) oxygen plants. 1–5. (2020)
2. Stein, F., Perry, M., Banda, G., Woolhouse, M., Mutapi, F.: Oxygen provision to fight COVID-19 in sub-Saharan Africa. *BMJ Glob Heal* (2020). <https://doi.org/10.1136/bmjgh-2020-002786>
3. Qadir, S., Li, D., Gu, Y., Yuan, Z., Zhao, Y., Wang, S., Wang, S.: Experimental and numerical analysis on the enhanced separation performance of a medical oxygen concentrator through two-bed rapid pressure swing adsorption. *Ind. Eng. Chem. Res.* (2021). <https://doi.org/10.1021/acs.iecr.1c00420>
4. Guan, W., Ni, Z., Hu, Y., Liang, W., Ou, C., He, J., Liu, L., Shan, H., Lei, C., Hui, D.S.C., Du, B., Li, L., Zeng, G., Yuen, K.Y., Chen, R., Tang, C., Wang, T., Chen, P., Li, S., Wang, J.L., Liang, Z., Peng, Y., Wei, L., Liu, Y., Hu, Y.H., Peng, P., Wang, J.M., Liu, J., Chen, Z., Li, G., Zheng, Z., Qiu, S., Luo, J., Ye, C., Zhu, S., Zhong, N.: Clinical characteristics of coronavirus disease 2019 in China. *N. Engl. J. Med.* (2020). <https://doi.org/10.1056/nejmoa2002032>
5. Ackley, M.W.: Medical oxygen concentrators: a review of progress in air separation technology. *Adsorption* (2019). <https://doi.org/10.1007/s10450-019-00155-w>
6. Fu, Q., Kansha, Y., Song, C., Tsutsumi, A.: An advanced cryogenic air separation process based on selfheat recuperation for CO₂ separation. *Energy Procedia* (2014). <https://doi.org/10.1016/j.egypro.2014.12.189>
7. Smith, A.R., Klosek, J.: A review of air separation technologies and their integration with energy conversion processes. *Fuel Process. Technol.* (2001). [https://doi.org/10.1016/S0378-3820\(01\)00131-X](https://doi.org/10.1016/S0378-3820(01)00131-X)

8. Ruthven, D.M., Farooq, S., Knaebel, K.S.: Pressure Swing Adsorption. Wiley, New York (1994)
9. Santos, J.C., Cruz, P., Regala, T., Magalhães, F.D., Mendes, A.: High-purity oxygen production by pressure swing adsorption. *Ind. Eng. Chem. Res.* (2007). <https://doi.org/10.1021/ie060400g>
10. Wu, C.W., Vemula, R.R., Kothare, M.V., Sircar, S.: Experimental study of a novel rapid pressure-swing adsorption based medical oxygen concentrator: effect of the adsorbent selectivity of N₂ over O₂. *Ind. Eng. Chem. Res.* (2016). <https://doi.org/10.1021/acs.iecr.5b04570>
11. Ferreira, D., Barcia, P., Whitley, R.D., Mendes, A.: Single-stage vacuum pressure swing adsorption for producing high-purity oxygen from air. *Ind. Eng. Chem. Res.* (2015). <https://doi.org/10.1021/acs.iecr.5b02151>
12. Jee, J.G., Lee, J.S., Lee, C.H.: Air separation by a small-scale two-bed medical O₂ pressure swing adsorption. *Ind. Eng. Chem. Res.* (2001). <https://doi.org/10.1021/ie0101011>
13. Santos, J.C., Portugal, A.F., Magalhães, F.D., Mendes, A.: Optimization of medical PSA units for oxygen production. *Ind. Eng. Chem. Res.* (2006). <https://doi.org/10.1021/ie0504809>
14. Epietang, F.E., Yang, X., Li, J., Wei, Y., Liu, Y., Yang, R.T.: Air separation sorbents: mixed-cation zeolites with minimum lithium and silver. *Chem. Eng. Sci.* (2019). <https://doi.org/10.1016/j.ces.2018.12.048>
15. Rege, S.U., Yang, R.T.: Limits for air separation by adsorption with LiX zeolite. *Ind. Eng. Chem. Res.* (1997). <https://doi.org/10.1021/ie9705214>
16. Rouquerol, F., Rouquerol, J., Sing, K.S.W., Llewellyn, P., Maurin, G.: Adsorption by Powders and Porous Solids Principles, Methodology and Applications. Academic Press, New York (2014)
17. Thommes, M., Kaneko, K., Neimark, A.V., Oliver, J.P., Rodriguez-Reinos, F., Rouquerol, J., Sing, K.S.W.: Physisorption of gases, with special reference to the evaluation of surface area and pore size distribution (IUPAC Technical Report). *Pure Appl. Chem.* (2015). <https://doi.org/10.1515/pac-2014-1117>
18. Bastos-Neto, M., Torres, A.E.B., Azevedo, D.C.S., Cavalcante, C.L.: Methane adsorption storage using microporous carbons obtained from coconut shells. *Adsorption* (2005). <https://doi.org/10.1007/s10450-005-6045-x>
19. Dreisbach, F., Lösch, H.W., Harting, P.: Highest pressure adsorption equilibria data: measurement with magnetic suspension balance and analysis with a new adsorbent/adsorbate-volume. *Adsorption* (2002). <https://doi.org/10.1023/A:1020431616093>
20. Moellmer, J., Moeller, A., Dreisbach, F., Glaeser, R., Staudt, R.: High pressure adsorption of hydrogen, nitrogen, carbon dioxide and methane on the metal-organic framework HKUST-1. *Microporous Mesoporous Mater.* (2011). <https://doi.org/10.1016/j.micromeso.2010.09.013>
21. Dreisbach, F., Staudt, R., Keller, J.U.: High pressure adsorption data of methane, nitrogen, carbon dioxide and their binary and ternary mixtures on activated carbon. *Adsorption* (1999). <https://doi.org/10.1023/A:1008914703884>
22. Park, Y., Moon, D.K., Kim, Y.H., Ahn, H., Lee, C.H.: Adsorption isotherms of CO₂, CO, N₂, CH₄, Ar and H₂ on activated carbon and zeolite LiX up to 10 MPa. *Adsorption* (2014). <https://doi.org/10.1007/s10450-014-9608-x>
23. Siqueira, R.M., Vilarrasa-García, E., Torres, A.E.B., Azevedo, D.C.S., Bastos-Neto, M.: Simple procedure to estimate mass transfer coefficients from uptake curves on activated carbons. *Chem. Eng. Technol.* (2018). <https://doi.org/10.1002/ceat.201800091>
24. Wilkins, N.S., Rajendran, A., Farooq, S.: Dynamic column breakthrough experiments for measurement of adsorption equilibrium and kinetics. *Adsorption* (2021). <https://doi.org/10.1007/s10450-020-00269-6>
25. Ding, Z., Han, Z., Fu, Q., Shen, Y., Tian, C., Zhang, D.: Optimization and analysis of the VPSA process for industrial-scale oxygen production. *Adsorption* (2018). <https://doi.org/10.1007/s10450-018-9956-z>
26. Rios, R.B., Correia, L.S., Bastos-Neto, M., Torre, A.E.B., Hatimondi, S.A., Ribeiro, A.M., Rodrigues, A.E., Cavalcante, C.L., Azevedo, D.C.S.: Evaluation of carbon dioxide–nitrogen separation through fixed bed measurements and simulations. *Adsorption* (2014). <https://doi.org/10.1007/s10450-014-9639-3>
27. Shafeeyan, M.S., Daud, W.M.A., Shamiri, A.: A review of mathematical modeling of fixed-bed columns for carbon dioxide adsorption. *Chem. Eng. Res. Des.* (2014). <https://doi.org/10.1016/j.cherd.2013.08.018>
28. Siqueira, R.M., Nascimento, J.F., Peixoto, H.R., Musse, A.: Carbon dioxide capture by pressure swing adsorption. *Energy Procedia* (2020). <https://doi.org/10.1016/j.egypro.2017.03.1355>
29. Nuhnen, A., Janiak, C.: A practical guide to calculate the isosteric heat/enthalpy of adsorption: via adsorption isotherms in metal-organic frameworks, MOFs. *Dalt Trans* (2020). <https://doi.org/10.1039/d0dt01784a>
30. Bird, R.B., Stewart, W.E., Lightfoot, E.N.: Transport Phenomena. Wiley, New York (2006)
31. Prausnitz, J.M., Rüdiger, N., Lichtenthaler, E.G.: Thermodynamic and Transport Properties of Coal Liquids. Prentice Hall, New Jersey (1987)
32. Ruthven, D.M.: Principles of Adsorption and Adsorption Processes. Wiley, New York (1984)
33. Talu, O.: Needs, status, techniques and problems with binary gas adsorption experiments. *Adv. Colloid Interface Sci.* (1998). [https://doi.org/10.1016/S0001-8686\(98\)00048-7](https://doi.org/10.1016/S0001-8686(98)00048-7)
34. Perry, R.H., Green, D.W., Maloney, F.: Perry's Chemical Engineers' Handbook. McGraw-Hill, New York (1997)
35. Wilke, C.R.: A viscosity equation for gas mixtures. *J. Chem. Phys.* (1950). <https://doi.org/10.1063/1.1747673>
36. Baksh, M.S.A., Kikkinides, E.S., Yang, R.T.: Lithium type X zeolite as a superior sorbent for air separation. *Sep. Sci. Technol.* (1992). <https://doi.org/10.1080/01496399208018880>
37. Wu, C.W., Kothare, M.V., Sircar, S.: Model analysis of equilibrium adsorption isotherms of pure N₂, O₂, and their binary mixtures on LiLSX zeolite. *Ind. Eng. Chem. Res.* (2014). <https://doi.org/10.1021/ie501750h>
38. Pan, M., Omar, H.M., Rohani, S.: Application of nanosize zeolite molecular sieves for medical oxygen concentration. *Nanomaterials* (2017). <https://doi.org/10.3390/nano7080195>
39. Ferreira, D., Magalhães, R., Bessa, J., Taveira, P., Sousa, J., Whitley, R.D., Mendes, A.: Study of AgLiLSX for single-stage high-purity oxygen production. *Ind. Eng. Chem. Res.* (2014). <https://doi.org/10.1021/ie500442r>
40. Sircar, S., Rao, M.B., Golden, T.C.: Fractionation of air by zeolites. *Stud. Surf. Sci. Catal.* (1999). [https://doi.org/10.1016/s0167-2991\(99\)80559-x](https://doi.org/10.1016/s0167-2991(99)80559-x)
41. Jee, J.G., Park, M.K., Yoo, H.K., Lee, K., Lee, C.H.: Adsorption and desorption characteristics of air on zeolite 5A, 10X, and 13X fixed beds. *Sep. Sci. Technol.* (2002). <https://doi.org/10.1081/SS-120014437>
42. Rao, V.R.: Adsorption based portable oxygen concentrator for personal medical applications. National University of Singapore (2011)

Publisher's Note Springer Nature remains neutral with regard to jurisdictional claims in published maps and institutional affiliations.

Springer Nature or its licensor (e.g. a society or other partner) holds exclusive rights to this article under a publishing agreement with the author(s) or other rightsholder(s); author self-archiving of the accepted manuscript version of this article is solely governed by the terms of such publishing agreement and applicable law.